Numerical experiment on data assimilation for geothermal doublets using production data and electromagnetic observations

Oudshoorn, Christiaan; Werthmüller, Dieter; Slob, Evert; Voskov, Denis

DOI
10.1190/GEO2023-0463.1

Publication date
2024

Document Version
Final published version

Published in
Geophysics

GEOPHYSICS, VOL. 89, NO. 6 (NOVEMBER-DECEMBER 2024); P. M227–M237, 8 FIGS.
10.1190/GEO2023-0463.1

DOI:10.1190/geo2023-0463.1

Numerical experiment on data assimilation for geothermal doublets using production data and electromagnetic observations

Christiaan Oudshoorn[1], Dieter Werthmüller[1], Evert Slob[1], and Denis Voskov[1]

ABSTRACT

The data assimilation process for geothermal reservoirs often relies on well data, which primarily offer insights into the immediate vicinity of the borehole. However, integrating geophysical methods can provide valuable information beyond well proximity, possibly enhancing reservoir predictions. Current methods of monitoring geothermal reservoirs struggle to maintain a good signal-to-noise ratio for deep reservoirs. Diffusive electromagnetic (EM) methods can be sensitive to the decreasing conductivity from heat extraction in geothermal reservoirs and offer promising additional value. To test their potential effectiveness, numerical examples are simulated. A scheme to incorporate diffusive EM observations into a data assimilation process for geothermal reservoirs is presented and implemented in this study. First, an ensemble of prior models representing the reservoir uncertainty is used to determine the moments of the resulting temperature field using a forward geothermal simulation. Subsequently, a conductivity model is calculated from the temperature field using an empirical relationship. The expected electric field response can then be simulated using an EM forward model. EM sources are placed on the surface around the expected cold plume location. The receiver is placed at reservoir depth. To assimilate the data, the ensemble smoother with multiple data assimilation method is used. The findings demonstrate that the incorporation of EM data provides valuable information regarding the temperature field. This improves the accuracy of the temperature forecast of the entire reservoir when combined with the localized data from the production well and, therefore, helps to resolve the complex migration of the cold front. These results highlight the monitoring potential of EM observations for geothermal reservoirs.

INTRODUCTION

Geothermal energy holds immense potential as a clean, renewable, and sustainable energy source (Hackstein and Madlener, 2021). Realizing the full benefits of this resource requires a profound comprehension of subsurface reservoirs containing geothermal energy, and numerical simulation stands as a powerful approach to achieving this understanding (Tian et al., 2024).

The calibration of physical reservoir models to match actual field measurements is fundamental to this endeavor. This process, commonly referred to as "history matching" or "data assimilation," aims to adjust the reservoir model to replicate the observed field measurements (Huseby et al., 2013; Wu et al., 2021). However, assimilation schemes rely solely on well data, such as temperature and borehole pressure, and suffer from limited information content, offering insights predominantly within the immediate vicinity of the boreholes (Zhang et al., 2020).

Geophysical measurements can address this limitation by providing valuable supplementary information concerning dynamic changes in the reservoir beyond the direct well proximity. In shallow geothermal applications, substantial progress has already been made in leveraging such measurements (Hermans et al., 2014). Specifically, time-lapse electrical resistivity tomography (ERT) has been effectively used in surface and borehole setups for shallow geothermal monitoring (Arato et al., 2015; Hermans et al., 2015; Lesparre et al., 2019). In addition, Ikard and Revil (2014) demonstrate the utility of self-potential measurements from a heat pulse to map the preferential flow paths in an experimental sandbox setup.

However, applying these methods to deep geothermal reservoirs at depths of several kilometers is challenging. Although advances in deep ERT have been made, a low signal-to-noise ratio (S/N) limits its effectiveness (Balasco et al., 2022).

Manuscript received by the Editor 8 August 2023; revised manuscript received 6 June 2024; published ahead of production 13 August 2024; published online 25 October 2024.
[1]Delft University of Technology, Delft, The Netherlands. E-mail: chrisxps@protonmail.com (corresponding author); d.werthmuller@tudelft.nl; e.c.slob@tudelft.nl; d.v.voskov@tudelft.nl.

DOI:10.1190/geo2023-0463.1

A promising alternative is the use of diffusive electromagnetic (EM) methods. In particular, magnetotellurics has shown potential for deep geothermal monitoring but allows for little control of the S/N, which limits its effectiveness in monitoring small temperature changes (Abdelfettah et al., 2018; Bretaudeau et al., 2021). Controlled-source diffusive EM methods may offer a sensitivity for subtle temperature changes that would allow for the monitoring of temperature changes in deep geothermal reservoirs (Eltayieb et al., 2023).

Tian et al. (2024) rely on proxy EM observations sampled around the entire reservoir for geothermal data assimilation. However, to measure the subtle temperature changes, the EM receivers have to be placed at reservoir depth. Due to the high cost associated with drilling wells, this severely limits the locations at which observation wells can be placed. To our knowledge, there is no existing literature exploring the potential impact of simulated diffusive EM measurements, which also account for the limited receiver locations within the geothermal data assimilation context.

The objective of this paper is to assess the feasibility of diffusive EM in the context of deep geothermal applications. We achieve this by integrating diffusive EM measurements into a data assimilation framework alongside the well data, aiming to enhance reservoir characterization. First, the method for creating a model ensemble is described, which is a collection of models that together describe the reservoir uncertainty. Thereafter, descriptions of the reservoir, rock physics, and EM forward models are given. Next, the method of data assimilation is described. Then, the moments of the model ensemble are given, and the EM survey setup is described. Finally, this model ensemble is incorporated into a data assimilation scheme incorporating diffusive EM observations to predict reservoir performance, and the results are evaluated and discussed.

THEORY

Ensemble generation

The initial phase of the workflow involves the generation of an ensemble to capture the uncertainty associated with reservoir parameters. In this paper, the focus is on the Delft sandstone member, which has considerable geothermal energy potential (Donselaar et al., 2015).

The ensemble is designed to reflect the characteristics of the Delft reservoir, which has a normally distributed porosity with a mean of 0.20 and a standard deviation of 0.09. Each member of the ensemble is comprised of a grid of 140×140 blocks, wherein each grid block measures 20 m $\times$ 20 m with a thickness of 100 m. This size was chosen to ensure that the temperature plume does not reach the model boundary within the simulation time. To create the ensemble members, a sequential Gaussian simulation is used. A total of 25 random grid blocks are assigned a random value from the aforementioned probability distribution for each realization. Values between these blocks are then estimated sequentially in a random order using a correlation defined by a spherical variogram:

$$c \cdot \mathrm{Sph}\left(\frac{h_d}{a_r}\right) = \begin{cases} c \cdot \left[1.5\frac{h_d}{a_r} - 0.5\left(\frac{h_d}{a_r}\right)^3\right], & \text{if } h \le a \\ c, & \text{if } h > a \end{cases}, \quad (1)$$

where h_d is the lag distance representing the distance between points, a_r is the range in m beyond which there is no correlation, and c is the sill (Deutsch and Journel, 1992). The sill represents the global maximum semivariance. In this paper, a range of 1000 m and a sill of one are used. The geostatistical package GeoStatPy for Python is used to facilitate this process (Pyrcz et al., 2021).

An empirical relationship is used to calculate the corresponding permeability, specifically

$$\begin{aligned} \log_{10}(\mu_h) = {} & (-3.523 \times 10^{-7}) \cdot (\phi \times 100)^5 \\ & + (4.278 \times 10^{-5}) \cdot (\phi \times 100)^4 \\ & - (1.723 \times 10^{-3}) \cdot (\phi \times 100)^3 \\ & + (1.896 \times 10^{-2}) \cdot (\phi \times 100)^2 \\ & + 0.333 \cdot (\phi \times 100) - 3.222, \end{aligned} \quad (2)$$

where μ_h is the hydraulic permeability in mD and ϕ is the porosity (Willems et al., 2020). Finally, the porosity was limited to be within 0.01 and 0.40 using truncation. This is done to ensure that the porosity values do not exceed the porosities seen in sandstone or cause simulation problems within the reservoir forward model. The injection well grid block, located on index $i_x = 40$ and $i_y = 70$, and the production well grid block, located on $i_x = 100$ and $i_y = 70$, are limited to having a permeability between 800 and 1000 mD.

Reservoir simulation

This paper uses the reservoir simulation approach based on the work by Khait and Voskov (2018) and Wang et al. (2020) and uses the Delft Advanced Research Terra Simulator (DARTS). This approach focuses on a two-phase thermal simulation with water, considering its governing equations and nonlinear formulations. However, this paper considers a low enthalpy system, and for this reason, the governing equations are adapted to account for a single phase.

The mass conservation equation of this system is described by

$$\frac{\partial}{\partial t}(\phi\rho) - \nabla \cdot (\rho u_d) + \rho\tilde{q} = 0, \quad (3)$$

and the energy conservation equation of this system is described by

$$\frac{\partial}{\partial t}[\phi\rho U + (1-\phi)U_r] \quad - \nabla \cdot (h\rho u_d) + \nabla \cdot (\kappa \nabla T) + h\rho\tilde{q} = 0, \quad (4)$$

where t represents the time in s, ρ represents the fluid density in kmol/m^3, represents the fluid source rate per unit volume in m^3/s, U indicates the specific fluid internal energy in kJ/kmol, U_r indicates the rock internal energy in kJ/m^3, h denotes the fluid enthalpy in kJ/kmol, κ represents the thermal conduction in W/m/K, and T represents the temperature in K.

Furthermore, the fluid Darcy velocity u_d in m/s, considering the gravity effects, can be defined as

$$u_d = \mathbf{K}\frac{1}{\mu}(\nabla P - \gamma \nabla D), \quad (5)$$

where $\mathbf{K}$ represents the permeability tensor of the media in mD, μ represents the fluid viscosity in Pa·s, P denotes the pressure in bars, γ represents the specific weight in N/m^3, and D signifies the depth

in m. The rock compressibility can be incorporated into the porosity using $\phi = \phi_0(1 + c_r(P - P_{\text{ref}}))$, where ϕ_0 represents the initial porosity, c_r represents the compressibility of the porous media in 1/bars, and P_{ref} is the reference pressure in bars.

In a geothermal system wherein the only component is water, pressure and enthalpy are considered as the primary variables in DARTS. To linearize the nonlinear system of equations, the Newton-Raphson method is adopted. The resulting system is expressed as

$$\mathbf{J}(\omega^k)(\omega^{k+1} - \omega^k) + r(\omega^k) = 0, \tag{6}$$

where $\mathbf{J}(\omega^k)$ is the Jacobian matrix and $r(\omega^k)$ is the residual, with k defining the iteration. The state variables of enthalpy and pressure are encapsulated and represented by ω. An initial time step of 10^{-3} days is used, with a maximum time step of 365 days, with the time step increasing by eight times as long as the solution is converging for the duration of the reservoir simulation.

To improve the computational process and flexibility of the nonlinear formulation, the operator-based linearization technique is used, as proposed by Khait and Voskov (2017). In this approach, the discretized mass and energy conservation equations are transformed into an operator form, separating the space- and state-dependent properties. The state-dependent operators are then parameterized in the space of nonlinear variables adaptively using a limited number of supporting points. This improves the speed and robustness of highly nonlinear reservoir simulation.

Rock-physics model

To model the EM response from the rock properties and dynamic changes, a rock-physics relationship is required, linking the reservoir parameters to conductivity. As hot water is extracted from the geothermal reservoir and cold water is injected, the temperature within the reservoir decreases. Over time, this forms a cold plume that progresses from the injection well to the production well.

Multiple studies have been conducted on measuring the change in conductivity as the temperature of a brine-saturated rock sample changes with varying degrees of complexity. Ucok et al. (1980) describe an empirical relationship linking the temperature and ions within the brine with conductivity, and Sen and Goode (1992) derive an empirical relationship that incorporates the inclusion of clay minerals.

For simplicity, however, the approach by Dresser Industries (1982) is used, which links salt concentration and temperature to electrical conductivity. Differences in the estimated conductivities among the previously mentioned methods are generally small, with the exception that the inclusion of clay minerals leads to a reduction in the change in conductivity with varying temperatures. In addition, the surface conductivity of clay is temperature dependent (Hayley et al., 2007). However, this surface conductivity contribution would be small for a reservoir filled with brine, as described in this paper.

Assuming that the main electrical conductive feature in the reservoir rock is the pore fluid, Archie's formula is used to determine the conductivity of the rock:

$$\sigma = \sigma_w \phi^m s_w^n, \tag{7}$$

where σ is the formation conductivity in S/m and σ_w is the brine conductivity in S. The saturation s_w is set to one as only one fluid is considered. Moreover, m and n are Archie's parameters and depend on the rock's compaction and saturation (Archie, 1942).

The brine conductivity σ_w can be determined by the empirical relationship:

$$\sigma_w = \left[\left(0.0123 + \frac{3647.5}{C_w^{0.955}}\right)\frac{82}{1.8T + 39}\right]^{-1}, \tag{8}$$

where C_w is the salt concentration in ppm (Dresser Industries, 1982). The salt concentration is assumed to remain constant at 100,000 ppm and the temperature is retrieved from the reservoir simulation to determine the conductivity at each grid cell.

If core sections are available, the relationship between temperature and conductivity also can be experimentally determined (Hermans et al., 2014). This would allow for a model that better matches the conductivity change of a reservoir with changing temperature.

EM modeling

This paper uses the emg3d 3D EM modeler, which is a Python package specifically suited for diffusion EM modeling and validated using other EM codes (Werthmüller et al., 2019, 2021). The response from the EM method is governed by Maxwell's equations (Stratton, 2015). In the presence of a current source $\mathbf{J}_s$ and under the diffusive field approximation, Maxwell's equations can be given as

$$\partial_t \mathbf{B}(\mathbf{x}, t) + \nabla \times \mathbf{E}(\mathbf{x}, t) = 0, \quad \nabla \times \mathbf{H}(\mathbf{x}, t) - \mathbf{J}_c(\mathbf{x}, t) = \mathbf{J}_s(\mathbf{x}, t), \tag{9}$$

where $\mathbf{J}_s$ is in A, $\mathbf{E}(\mathbf{x}, t)$ is the electrical field in V/m, and $\mathbf{H}(\mathbf{x}, t)$ is the magnetic field in A/m (Werthmüller et al., 2019).

The conduction current is defined such that it obeys Ohm's law as

$$\mathbf{J}_c = \sigma(\mathbf{x})\mathbf{E}(\mathbf{x}, t), \tag{10}$$

and the magnetic induction is defined as

$$\mathbf{B}(\mathbf{x}, t) = \mu_0 \mathbf{H}(\mathbf{x}, t), \tag{11}$$

where μ_0 is the vacuum magnetic permeability in H/m.

In this paper, the relative permeability μ_r is set to one. Eliminating the magnetic field from equation 9 yields the second-order parabolic system of equations given as

$$\sigma \partial_t \mathbf{E} + \nabla \times \mu_0^{-1} \nabla \times \mathbf{E} = -\partial_t \mathbf{J}_s. \tag{12}$$

Using the Fourier transform, the electrical field $\mathbf{E}(\mathbf{x}, t)$ can be brought into the frequency domain, yielding

$$i\omega\sigma\hat{\mathbf{E}} + \nabla \times \mu_0^{-1}(\nabla \times \hat{\mathbf{E}}) = -i\omega\hat{\mathbf{J}}_s. \tag{13}$$

Finally, a perfectly electrically conducting boundary can be used such that $\mathbf{n} \times \mathbf{E} = 0$ and $\mathbf{n} \cdot \mathbf{H} = 0$, where $\mathbf{n}$ is the outward normal vector on the boundary of the computational domain.

The current source $\mathbf{J}_s$ is a 1 m long 1 A electric dipole, and the conductivity model $\sigma(\mathbf{x})$ is retrieved from the reservoir model. The electric field $\mathbf{E}$ is the only unknown that has to be solved

(Werthmüller et al., 2019). Finally, a sampling operator $\mathbf{S}(\cdot)$ that samples the electric field $\mathbf{E}$ at receiver locations to obtain the observed data $\mathbf{d}_{\text{obs}}$ is given by

$$\mathbf{d}_{\text{obs}} = |\mathbf{S}(\mathbf{x}_s, \mathbf{x}_r)|, \tag{14}$$

where $\mathbf{x}_s$ represents the source locations and $\mathbf{x}_r$ represents the receiver locations. The modulus is taken to obtain the amplitude of the electric field $\mathbf{E}$ and to avoid complex numbers in the measured data.

The EM forward model requires a 3D grid, whereas the conductivity model has two dimensions. For compatibility, the conductivity model is extrapolated into a 3D grid. Buffer cells are added surrounding the original 2D model and given a conductivity of 1 S/m. The number of buffer cells in each direction is calculated based on the frequency and the aforementioned buffer cell conductivity. This ensures that the conductivity model is at least one wavelength from the boundary to avoid boundary effects due to boundary conditions.

Data assimilation scheme

The ensemble smoother with multiple data assimilation (ES-MDA) method (Emerick and Reynolds, 2013) is used in this paper to improve model predictions by incorporating observed data. ES-MDA uses an ensemble of models to capture inherent uncertainty, advancing them in time using model equations, reflecting the range of potential outcomes due to uncertainty in the initial conditions and model parameters. This approach focuses on parameter estimation leveraging the stability of reservoir simulation models in relation to rock reservoir fields.

To update the model, the ES-MDA method considers several factors. These include the discrepancy between the predicted and measured data, the cross-covariance between the model parameters and the predicted data, the autocovariance of the predicted data, and the covariance matrix of the observed measurement orders.

This process constitutes the ensemble smoother component of ES-MDA. However, this approach can be seen as equivalent to a single Gauss-Newton iteration. To potentially achieve better convergence, ES-MDA incorporates multiple data assimilation by inflating the covariance matrix associated with measurement errors. By performing several smaller iterations instead of one large correction, the method aims to refine the parameter estimation further, ultimately improving the convergence of the assimilation process.

The ES-MDA analysis equation is given by

$$\mathbf{m}_j^a = \mathbf{m}_j^f + \mathbf{C}_{\text{MD}}^f(\mathbf{C}_{\text{DD}}^f + \alpha_i \mathbf{C}_{\text{D}})^{-1}(\mathbf{d}_{\text{uc},j} - \mathbf{d}_j^f), \tag{15}$$

for $j = 1, 2, \ldots, N_e$, where N_e is the number of ensemble realizations. Moreover, $\mathbf{C}_{\text{MD}}$ represents the cross-covariance matrix of the model parameters $\mathbf{m}$ and the predicted data $\mathbf{d}$, $\mathbf{C}_{\text{DD}}$ is the $N_d \times N_d$ autocovariance matrix of the predicted data with N_d representing the number of observed data, and $\mathbf{C}_{\text{D}}$ is the $N_d \times N_d$ covariance matrix of measurement errors. Here, α_i is the magnitude of perturbation applied to the observations. The superscripts a and f are the analysis and forecast, respectively. In this paper, porosity is taken as the model parameter, and temperature and pressure at the production well and vertical electric field amplitude at the receiver are taken as the observed data. The vertical electric field amplitude measurements, in particular, are also scaled by a constant to bring them closer to the magnitude of the other production well measurements.

Finally, $\mathbf{d}_{\text{uc}}$ is defined as

$$\mathbf{d}_{\text{uc}} = \mathbf{d}_{\text{obs}} + \sqrt{\alpha_i}\mathbf{C}_{\text{D}}^{1/2}\mathbf{Z}_d, \tag{16}$$

where $\mathbf{d}_{\text{obs}}$ is the observed data and $\mathbf{Z}_d$ is an $N_d \times N_e$ matrix composed of random samples drawn from a normal Gaussian distribution. It has to satisfy the condition that $\sum_{i=1}^{N_a}(1/\alpha_i) = 1$, but it is otherwise a user-set parameter.

The ES-MDA algorithm can be summarized as follows:

1) Determine the number of data assimilations N_a and the coefficients α_i for $i = 1, \ldots, N_a$.
2) For each data assimilation iteration $i = 1$ to N_a:
   - Run the entire ensemble from time 0.
   - Perturb the observations with equation 16.
   - Update the ensemble using equation 15.

RESULTS

Ensemble moments and EM survey

To measure the subtle changes in temperature associated with geothermal extraction within the reservoir, the receivers have to be placed at reservoir depth (Eltayieb et al., 2023). Placing receivers in boreholes at the desired depth is a costly solution. Therefore, careful consideration must be given to receiver placement to maximize the benefits from each observation well. Because transmitting current to reservoir depth is difficult, the sources are positioned on the surface. Moreover, the receivers should have a 300 m distance from any well with a steel casing to avoid interference with the EM signal (Eltayieb et al., 2023). The casing should be made of highly resistive material with no magnetization to avoid a significant impact on the measurements.

A prior ensemble consisting of 100 realizations is used. One additional ensemble member is used as the reference model. To simulate the conductivity field before and after injection, each ensemble member was simulated for 25 years using the reservoir forward model with an initial temperature of 348.15 K and an injection temperature of 308.15 K, thermal conductivity of 2.1 W/m/K, and an injection rate of 0.0579 m^3/s. The injection well is placed at $x = 800$ and $y = 1400$ m, and the production well is positioned at $x = 2000$ and $y = 1400$ m.

Figure 1a and 1b shows the resulting conductivity field of the reference model before and after the simulation. Figure 1c and 1d shows the conductivity and temperature difference. Here, it is seen that as the cold front infiltrates the reservoir, it leaves an imprint in the conductivity field of approximately 0–1 S/m. Because the pore fluid is the primary conductor, the decrease in conductivity also reflects the porosity.

The corresponding vertical electric field amplitudes are shown in Figure 2a and 2b, respectively. The ratio of the two electrical fields is shown in Figure 2c to highlight better the impact of conductivity changes on the vertical electric field amplitude. The decreased conductivity leads to a modified vertical electric field amplitude because the electric field $\mathbf{E}$ is allowed to penetrate deeper into the reservoir due to reduced current loss in highly conductive zones.

Figure 3a and 3b shows the mean of the temperature field and the corresponding mean vertical electric field amplitude of the entire ensemble before and after the simulation, respectively.

DOI:10.1190/geo2023-0463.1

Figure 3c and 3d shows the standard deviation of the temperature field and the corresponding standard deviation of the vertical electric field amplitude, respectively. Because the ensemble was generated using a Gaussian assumption, the mean and standard deviation of the temperature field and vertical electrical field ensemble also show a Gaussian pattern. In contrast, the reference model shows a more complex flow of the cold front to the production well.

The EM survey is positioned around the area with a changed vertical electric field amplitude caused by the cold front. Nine source locations were used at the following x- and y-coordinates: (250, 400), (250, 1400), (250, 2400), (850, 400), (850, 1400), (850, 2400), (1450, 400), (1450, 1400), and (1450, 2400). All source locations were placed on the surface at $z = 0$ m.

The observation well was placed at $x = 1400$ m and $y = 1400$ m. Because a 2D model was used, only one receiver was placed at $z = -2050$ m. From Figures 3b and 3d, it can be seen that this receiver location has a mean change of approximately 10% due to the cold plume and a standard deviation of approximately 12% after a 25 year period. It is important to place the observation well and EM receiver in a location with a large amount of deviation. Larger measurements relative to the noise level increase the magnitude of the model update within the data assimilation. A schematic representation of the survey is shown in Figure 4.

To further improve the impact of the observation well on uncertainty reduction, the observation well could be equipped with a wider array of geophysical sensing equipment. In this case, a Bayesian optimal experimental design could be applied to determine the optimal location of the observation well and sources for multiple geophysical methods at once (Thibaut et al., 2022).

Data assimilation of diffusive EM data

The data assimilation training spanned 25 years with a five year measurement interval, which was chosen due to computational considerations and measurement consistency. After the training period, the simulations had a prediction period of 25 years. Temperature and pressure measurements were sampled at the production well during the training period. The vertical electrical field amplitude at the receiver was sampled at the same five year intervals, scaled by multiplying it by 10^{14}. This scaling is applied to give the EM observations the same order of magnitude as the well observations. The change over time of all the observations is also used, calculated by taking the change in observations divided by the change in time between consecutive sampling times.

Reference production well observations were given a uniform noise of 3% based on the original observations, which are typically found in the literature (Wu et al., 2021). For temperature, this percentage is applied to degrees Celsius rather than Kelvin. Due to the depth of the EM receiver, the measurements are unlikely to be significantly affected by anthropogenic noise. Moreover, due to the relatively short distance between the source and the receiver, the measurements can be kept above the noise floor. To still account for other noise sources, such as survey repeatability errors, the EM measurements were given a uniform noise of 1% based on the EM measurements (Eltayieb et al., 2023).

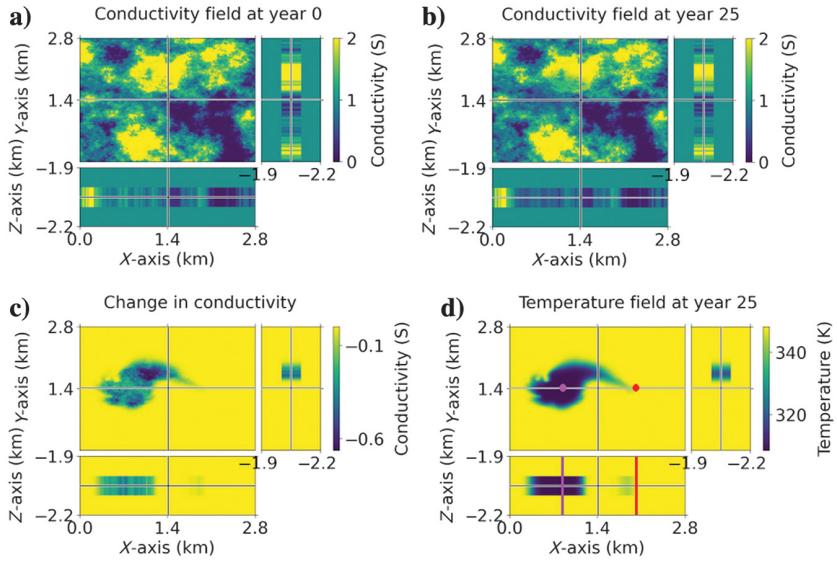

Figure 1. Changes in the conductivity field and temperature field over time. (a) The conductivity field at year 0 in S/m, (b) the conductivity field at year 25 in S/m, (c) the difference between both conductivity fields in S/m, and (d) the temperature field at year 25 in K. The temperature field also has the injection well to the left marked with purple and the production well to the right marked with red.

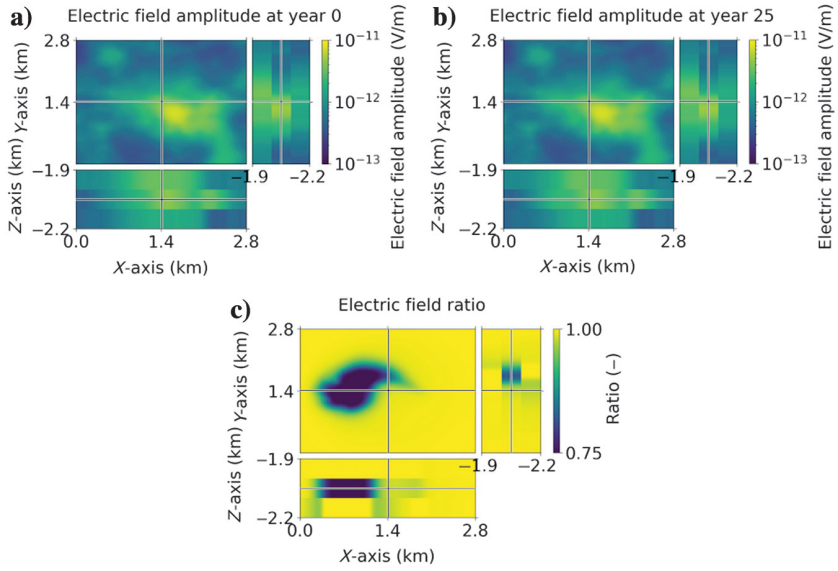

Figure 2. Vertical electric field amplitude of both conductivity fields of Figure 1, with the source placed at $x = 1400$ and $y = 1400$. (a) The vertical electric field amplitude in V/m at year 0, (b) the electric field amplitude in V/m at year 25, and (c) the ratio between the vertical electric field amplitude before and after 25 years.

The data assimilation process is comprised of six steps, with the α_i values being 1/0.02, 1/0.03, 1/0.1, 1/0.15, 1/0.3, and 1/0.4. This causes each subsequent data assimilation iteration to have a smaller covariance matrix, allowing for increasingly larger corrections.

Three different scenarios were tested: one wherein only production well observations were used, one wherein the production well and EM observations were used, and one wherein only the EM observations were used. The respective temperature results at the production well are shown in Figure 5a–5c.

The integration of the EM observations has significantly reduced the uncertainty of the temperature at the production well. However, the accuracy has decreased. The result using only well observations barely converged when compared with the prior ensemble. This is likely due to the noise level in the well data being close to the change in the temperature at the production well during the training period. To demonstrate the effect of more impactful well measurements, two additional simulations were performed using a production well noise level of 0.1%, which allows for the observations to be below the noise level. The results for scenarios using only production well observations and production well and EM observations are shown in Figure 5d and 5e. Figure 5d shows a significant reduction in uncertainty, better alignment with observations, and increased accuracy. In contrast, Figure 5e is less accurate and shows a smaller reduction in uncertainty. This is likely due to the larger number of EM observations compared with well measurements, causing ES-MDA to prioritize the EM observations. Nevertheless, an improvement is observed compared with the prior ensemble and the results shown in Figure 5b. Finally, ES-MDA has not fully converged to the expected noise level within the training period. This is likely due to the low number of observations during the training period, making it difficult for ES-MDA to converge.

The mean of the posterior temperature field for all three scenarios is shown in Figure 6a–6c, and the standard deviation is shown in Figure 6d–6f. The difference between the posterior mean and the reference temperature field is shown in Figure 6g–6i. The root mean square of the difference between the mean and the reference temperature field for the three cases is 3.62, 2.10, and 2.49.

Likewise, the same figures using 0.1% production well noise are shown in Figure 7a and 7d for the mean temperature field, Figure 7b and 7e for the standard deviation, and Figure 7c and 7f for the difference between the posterior mean and the reference temperature field. The root mean square of the difference between the mean and the reference temperature field was 3.55 for the case when using only well observations and 1.88 when the well and EM observations were used.

The temperature plume prediction is significantly improved by the inclusion of EM observations. Moreover, the standard deviation is also significantly reduced. Using well and EM observations gives additional improvements to the mean and standard deviation when compared with the scenario using only

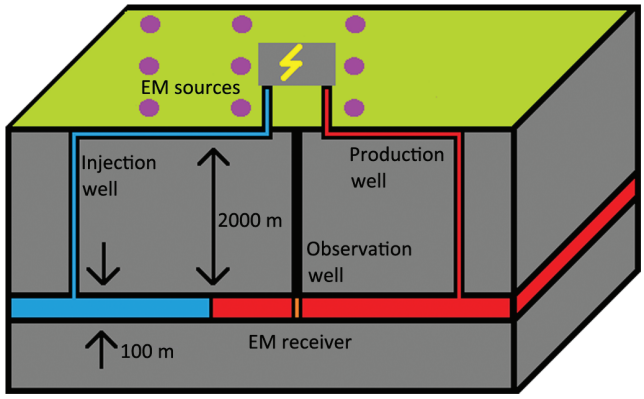

Figure 4. Schematic representation of the survey setup. Indicated are the geothermal doublet, observation well with the EM receiver, and multiple surface EM sources.

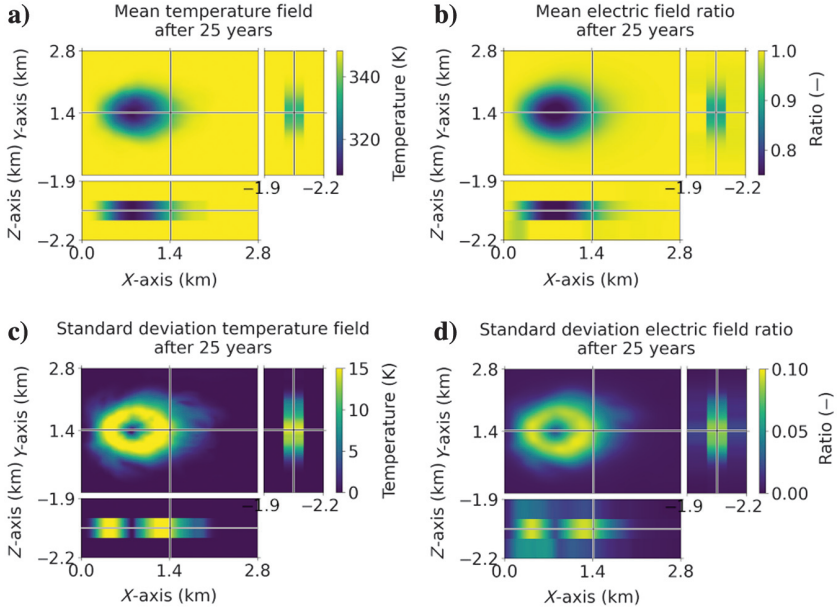

Figure 3. (a) Mean temperature field in K and (b) vertical electric field amplitude in V/m of the entire ensemble. (c) The standard deviation of the temperature field in K and (d) vertical electric field amplitude in V/m of the entire ensemble. The source was placed at $x = 1400$ and $y = 1400$, and the plots were taken at year 25.

EM observations. Most importantly, the moments of the temperature plume when EM observations are used resemble the cold plume migration of the reference model. In addition, the plots using 0.1% production well noise demonstrate the limited effect of production well observations on the entire temperature field. Despite the significant decrease in noise, the temperature field remains similar, with only the plots using the production well and EM observations showing some marginal differences.

Results for the mean of the porosity field for all three scenarios are shown in Figure 8a–8c, and the standard deviation is shown in Figure 8d–8f. Finally, the absolute difference between the mean and reference porosity field is shown in Figure 8g–8i. The root mean square of the difference between the mean and reference porosity field for the three cases is 0.07, 0.08, and 0.08. Due to the porosity field plots for the 0.1% scenarios being largely the same, they have been omitted for brevity.

The mean of the porosity field is more heterogeneous with the inclusion of EM observations. Moreover, a region of low porosity is formed in the center and bottom-left quadrant of the porosity field. This region also has a relatively low standard deviation. This forces the cold front to migrate in a way similar to the reference model. Notably, EM observations do not significantly improve the difference between the mean and reference porosity field when compared with the situation wherein only well observations are used. However, they do cause the porosity field to have features that cause the temperature field to migrate in a way similar to the reference model. The porosity field moments using only the observation well measurements closely match the moments used to create the ensemble.

The results indicate that EM observations are able to resolve complex cold plume behavior accurately. Moreover, they are better able to reduce uncertainty within the reservoir when compared with relying on production well observations alone. The inclusion of well and EM observations further reduces the uncertainty even more. These results indicate that EM observations could be useful in reservoirs where the cold flume migration shows great variability. This could be especially useful in complex reservoirs such as fluvial systems.

DISCUSSION

The integration of EM observations into the data assimilation process significantly reduced the uncertainty and increased the accuracy of the temperature predictions of the reservoir. Moreover, they also decrease the uncertainty at the production well. These results indicate that EM observations can provide valuable supplementary data, improving the accuracy of the temperature field predictions in geothermal reservoirs. The integration of these observations helped to capture the cold plume migration better, highlighting their sensitivity to temperature-induced conductivity changes even at the simulated depth of 2 km. The simulations with lower noise levels in well data demonstrated that more precise well measurements could further enhance the assimilation process, though the abundance of EM data requires careful balancing to avoid prioritization issues. Finally, EM observations seem to mainly improve the accuracy of the temperature predictions of the entire reservoir rather than the localized improvements at the well seen

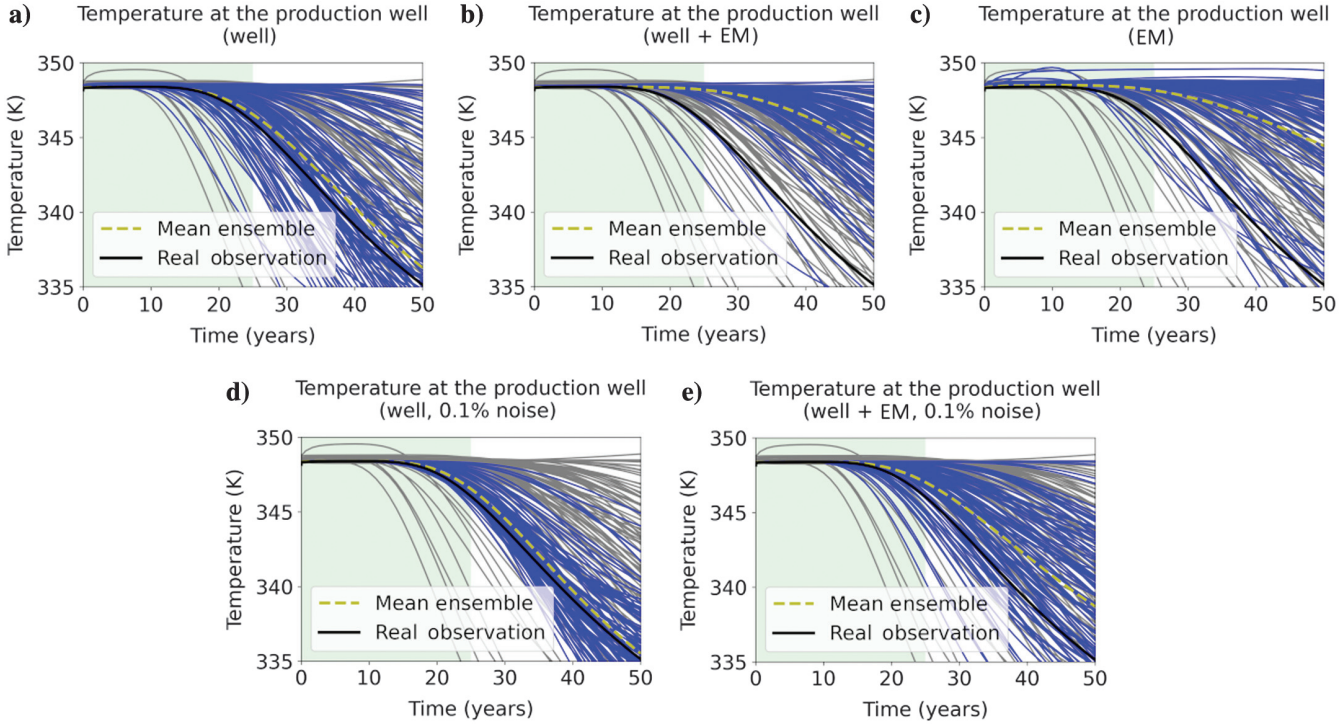

Figure 5. Data assimilation results using either the production well observations, well and EM observations, or only EM observations. Results for (a) temperature at the production well using only well observations, (b) using well and EM observations, and (c) using only EM observations. Results (d) using 0.1% for the well data noise data using only the well observations and (e) the well and EM observations are also shown. The green segment of the production well temperature plot represents the data assimilation training time, and the white area represents the prediction time. The gray lines represent the prior ensemble, and the blue lines represent the ensemble after data assimilation. The black line represents the reference model observation, and the dotted yellow line represents the ensemble mean.

from including observation well data. The enhancement of temperature field predictions is particularly important in complex geologic settings where traditional well data may be insufficient. The improved resolution of cold plume behavior and reduced uncertainty can lead to more efficient and effective geothermal energy extraction and management.

The largest limitation of the study is the use of Gaussian 2D models, which do not account for vertical heterogeneity or variations in temperature and conductivity that could influence the results. ES-MDA has become the state of the art for data assimilation for history matching in recent years (Toma and Sebacher, 2022). However, the requirement for Gaussian ensemble members in the ES-MDA method restricts the complexity and realism of the reservoir models (Emerick and Reynolds, 2013). The study also did not fully explore the impact of the overburden's conductivity, which could affect the data assimilation process as well. Various methods exist to improve the complexity and accuracy of the models used. Truncated Gaussian can be used to increase the complexity of the models further while maintaining Gaussianity (Astrakova and Oliver, 2014). Moreover, deep-learning methods such as generative adversarial networks can be used to reparameterize non-Gaussian models into a low-dimensional space, which allows ES-MDA to perform model updates (Bao et al., 2020). Relaxing the Gaussian requirement would allow for alternative methods to generate the ensemble, such as multipoint geostatistics, which would enable more complex and realistic models, such as channelized reservoirs (Mariethoz and Caers, 2014). Finally, alternative methods for data assimilation exist in the literature, such as adjoint-based data assimilation or gradual deformation, which are able to function on non-Gaussian models (Benoit et al., 2021; Tian et al., 2024).

The results in this paper demonstrate the potential of diffusive EM to monitor deep geothermal reservoirs. This allows for it to be a potential alternative to ERT or magnetotellurics, which have been used to monitor geothermal reservoirs in the past but struggle to monitor deeper geothermal reservoirs. Future studies should explore the use of more realistic 3D models to capture vertical heterogeneity. Moreover, research is required to determine better strategies for data assimilation to allow for more realistic geologies for geothermal reservoirs. Finally, the inclusion of other geophysical methods could be experimented with to enhance the predictions of geothermal reservoirs further.

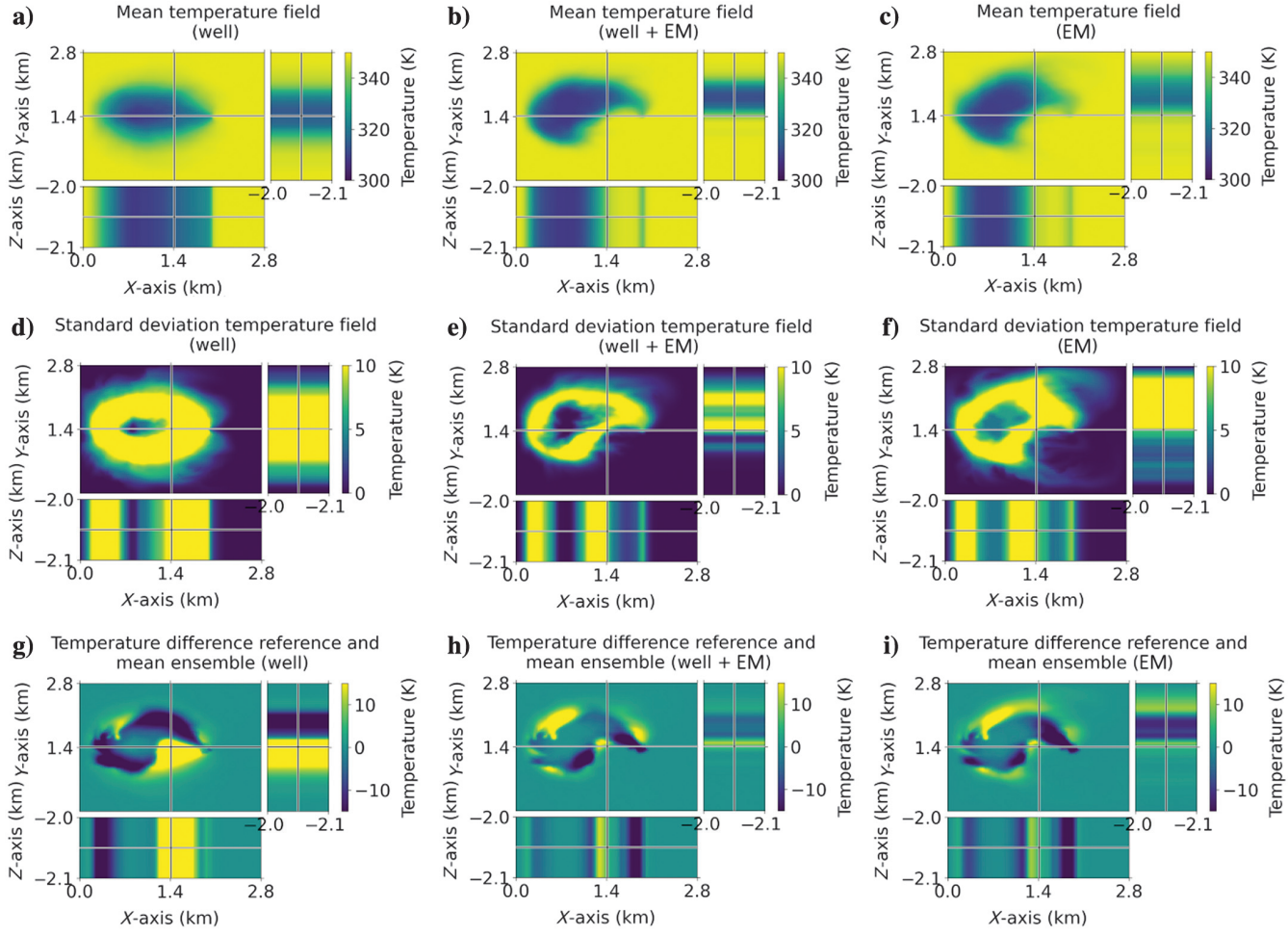

Figure 6. Data assimilation results using the production well observations, the well and EM observations, or only the EM observations. (a–c) Mean temperature field, (d–f) standard deviation of the temperature field of the entire ensemble, and (g–i) difference between the mean of the ensemble and the reference model. All plots are taken at year 50.

DOI:10.1190/geo2023-0463.1

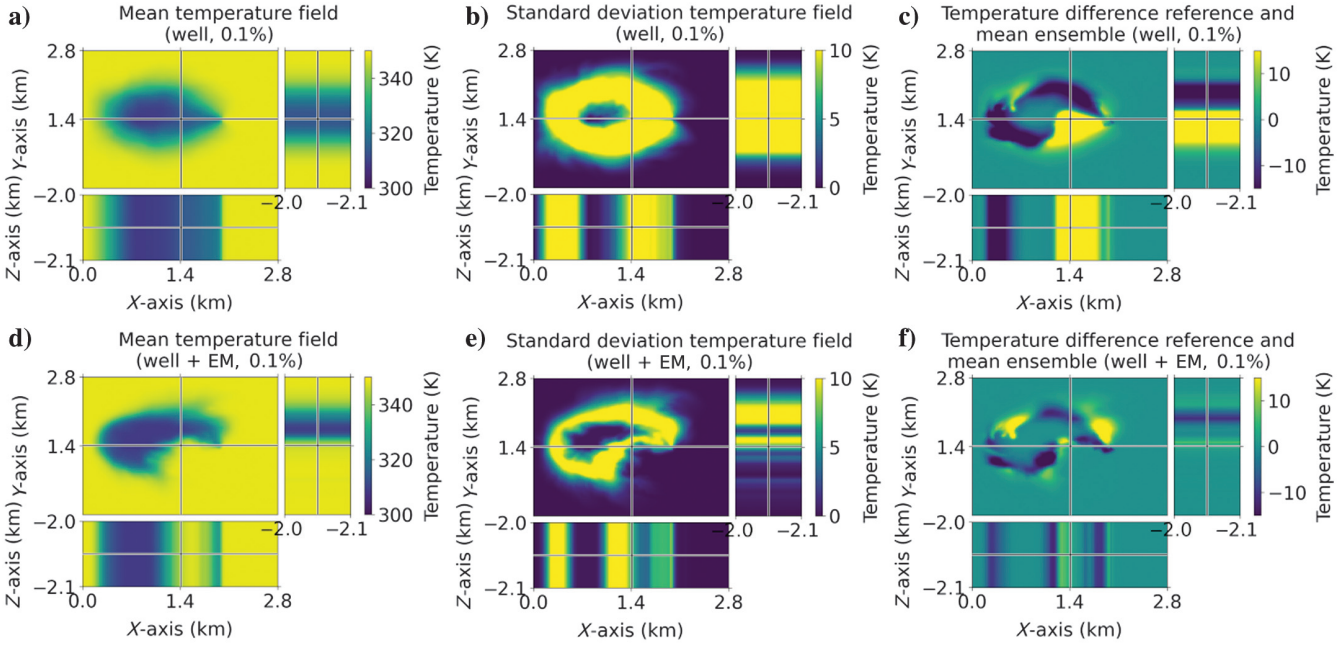

Figure 7. Data assimilation results using either the production well observations or the well and EM observations using 0.1% production well noise. (a and d) Mean temperature field, (b and e) the standard deviation of the temperature field of the entire ensemble, and (c and f) the difference between the mean of the ensemble and reference model. All plots are taken at year 50.

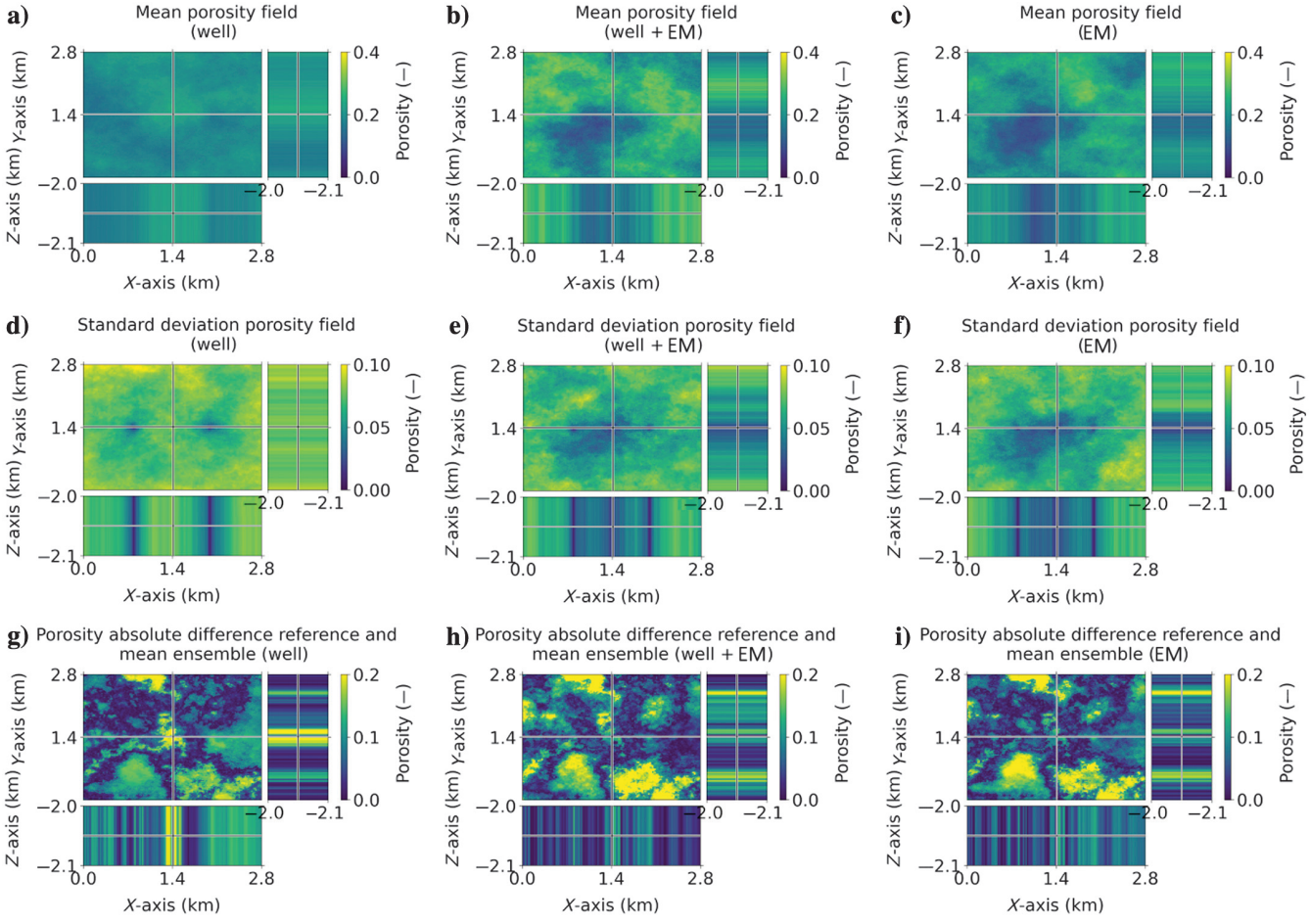

Figure 8. Data assimilation results using the production well observations, well and EM observations, or only EM observations. (a–c) Mean porosity field, (d–f) standard deviation of the porosity field of the entire ensemble, and (g–i) absolute difference between the mean of the ensemble and reference model. All plots are taken at year 50.

CONCLUSION

We have demonstrated the effect of integrating EM observation data into a data assimilation scheme for geothermal reservoir forecasting of the temperature distribution in a numerical example. The numerical experiment results have demonstrated that the change in conductivity caused by the cold water plume is substantially sufficient to be effectively quantified using diffusive EM measurements in a borehole with several electric current source locations on the ground surface. Moreover, by incorporating the temporal evolution of the vertical electric field amplitude into the data assimilation scheme, we have observed improvements in the accuracy of the temperature forecasts. Specifically, the incorporation of EM data allows for better mapping of the spatial temperature distribution, which, when combined with the more localized information from the production well observations, significantly reduces the uncertainty in the reservoir. Consequently, this method holds the potential to provide more precise constraints on the lifetime predictions of geothermal doublets and monitoring of geothermal reservoirs. To further explore the viability of using EM observations and applicability for real-life data, more research in determining a suitable data assimilation strategy and representative ensemble is required.

ACKNOWLEDGMENTS

The authors would like to thank M. Eltayieb, A. Daniildis, and A. Novikov for fruitful discussions and support regarding various aspects of the forward models. Special thanks to G. S. Seabra for providing his code and extensive help with the data assimilation scheme.

DATA AND MATERIALS AVAILABILITY

Data associated with this research are available and can be obtained by contacting the corresponding author.

REFERENCES

Abdelfettah, Y., P. Sailhac, H. Larnier, P.-D. Matthey, and E. Schill, 2018, Continuous and time-lapse magnetotelluric monitoring of low volume injection at Rittershoffen geothermal project, northern Alsace — France: Geothermics, **71**, 1–11, doi: 10.1016/j.geothermics.2017.08.004.

Arato, A., J. Boaga, C. Comina, M. De Seta, E. Di Sipio, A. Galgaro, N. Giordano, and G. Mandrone, 2015, Geophysical monitoring for shallow geothermal applications — Two Italian case histories: First Break, **33**, 75–79, doi: 10.3997/1365-2397.33.8.82010.

Archie, G. E., 1942, The electrical resistivity log as an aid in determining some reservoir characteristics: Transactions of the AIME, **146**, 54–62, doi: 10.2118/942054-G.

Astrakova, A., and D. Oliver, 2014, Conditioning truncated pluri-Gaussian models to facies observations in ensemble-Kalman-based data assimilation: Mathematical Geosciences, **47**, 345–367, doi: 10.1007/s11004-014-9532-3.

Balasco, M., V. Lapenna, E. Rizzo, and L. Telesca, 2022, Deep electrical resistivity tomography for geophysical investigations: The state of the art and future directions: Geosciences, **12**, 438, doi: 10.3390/geosciences12120438.

Bao, J., L. Li, and F. Redoloza, 2020, Coupling ensemble smoother and deep learning with generative adversarial networks to deal with non-Gaussianity in flow and transport data assimilation: Journal of Hydrology, **590**, 125443, doi: 10.1016/j.jhydrol.2020.125443.

Benoit, N., D. Marcotte, and J. Molson, 2021, Stochastic correlated hydraulic conductivity tensor calibration using gradual deformation: Journal of Hydrology, **594**, 125880, doi: 10.1016/j.jhydrol.2020.125880.

Bretaudeau, F., F. Dubois, S.-G. Bissavetsy Kassa, N. Coppo, P. Wawrzyniak, and M. Darnet, 2021, Time-lapse resistivity imaging: CSEM-data 3-D double-difference inversion and application to the Reykjanes geothermal field: Geophysical Journal International, **226**, 1764–1782, doi: 10.1093/gji/ggab172.

Deutsch, C., and A. Journel, 1992, GSLIB: Geostatistical software library and user's guide: Oxford University Press.

Donselaar, M., R. Groenenberg, and D. Gilding, 2015, Reservoir geology and geothermal potential of the Delft sandstone member in the West Netherlands basin: Proceedings World Geothermal Congress.

Dresser Industries, 1982, Well logging and interpretation techniques: The course for home study: Dresser Atlas.

Eltayieb, M., D. Werthmüller, G. Drijkoningen, and E. Slob, 2023, Feasibility study of controlled-source electromagnetic method for monitoring low-enthalpy geothermal reservoirs: Applied Sciences, **13**, 9399, doi: 10.3390/app13169399.

Emerick, A. A., and A. C. Reynolds, 2013, Ensemble smoother with multiple data assimilation: Computers & Geosciences, **55**, 3–15, doi: 10.1016/j.cageo.2012.03.011.

Hackstein, F. V., and R. Madlener, 2021, Sustainable operation of geothermal power plants: Why economics matters: Geothermal Energy, **9**, 1–30, doi: 10.1186/s40517-021-00183-2.

Hayley, K., L. R. Bentley, M. Gharibi, and M. Nightingale, 2007, Low temperature dependence of electrical resistivity: Implications for near surface geophysical monitoring: Geophysical Research Letters, **34**, L18402, doi: 10.1029/2007GL031124.

Hermans, T., F. Nguyen, T. Robert, and A. Revil, 2014, Geophysical methods for monitoring temperature changes in shallow low enthalpy geothermal systems: Energies, **7**, 5083–5118, doi: 10.3390/en7085083.

Hermans, T., S. Wildemeersch, P. Jamin, P. Orban, S. Brouyère, A. Dassargues, and F. Nguyen, 2015, Quantitative temperature monitoring of a heat tracing experiment using cross-borehole ERT: Geothermics, **53**, 14–26, doi: 10.1016/j.geothermics.2014.03.013.

Huseby, O., R. Valestrand, G. Nævdal, and J. Sagen, 2013, Natural and conventional tracers for improving reservoir models using the EnKF approach: SPE Journal, **15**, 1047–1061, doi: 10.2118/121190-MS.

Ikard, S., and A. Revil, 2014, Self-potential monitoring of a thermal pulse advecting through a preferential flow path: Journal of Hydrology, **519**, 34–49, doi: 10.1016/j.jhydrol.2014.07.001.

Khait, M., and D. Voskov, 2017, Operator-based linearization for general purpose reservoir simulation: Journal of Petroleum Science and Engineering, **157**, 990–998, doi: 10.1016/j.petrol.2017.08.009.

Khait, M., and D. Voskov, 2018, Operator-based linearization for efficient modeling of geothermal processes: Geothermics, **74**, 7–18, doi: 10.1016/j.geothermics.2018.01.012.

Lesparre, N., T. Robert, F. Nguyen, A. Boyle, and T. Hermans, 2019, 4D electrical resistivity tomography (ERT) for aquifer thermal energy storage monitoring: Geothermics, **77**, 368–382, doi: 10.1016/j.geothermics.2018.10.011.

Mariethoz, G., and J. Caers, 2014, Multiple-point geostatistics: Stochastic modeling with training images: John Wiley & Sons, Ltd.

Pyrcz, M., H. Jo, A. Kupenko, W. Liu, A. Gigliotti, T. Salomaki, and J. Santos, 2021, GeostatsPy python package: PyPI, Python package index, https://pypi.org/project/geostatspy/, accessed 1 August 2023.

Sen, P. N., and P. A. Goode, 1992, Influence of temperature on electrical conductivity on shaly sands: Geophysics, **57**, 89–96, doi: 10.1190/1.1443191.

Stratton, J., 2015, Electromagnetic theory: Wiley, IEEE Press Series on Electromagnetic Wave Theory.

Thibaut, R., N. Compaire, N. Lesparre, M. Ramgraber, E. Laloy, and T. Hermans, 2022, Comparing well and geophysical data for temperature monitoring within a Bayesian experimental design framework: Water Resources Research, **58**, e2022WR033045, doi: 10.1029/2022WR033045.

Tian, X., O. Volkov, and D. Voskov, 2024, An advanced inverse modeling framework for efficient and flexible adjoint-based history matching of geothermal fields: Geothermics, **116**, 102849, doi: 10.1016/j.geothermics.2023.102849.

Toma, S.-A., and B. Sebacher, 2022, Bridging deep convolutional autoencoders and ensemble smoothers for improved estimation of channelized reservoirs: Mathematical Geosciences, **54**, 903–939, doi: 10.1007/s11004-022-09997-7.

Ucok, H., I. Ershaghi, and G. R. Olhoeft, 1980, Electrical resistivity of geothermal brines: Journal of Petroleum Technology, **32**, 717–727, doi: 10.2118/7878-PA.

Wang, Y., D. Voskov, M. Khait, and D. Bruhn, 2020, An efficient numerical simulator for geothermal simulation: A benchmark study: Applied Energy, **264**, 114693, doi: 10.1016/j.apenergy.2020.114693.

Werthmüller, D., W. A. Mulder, and E. C. Slob, 2019, emg3d: A multigrid solver for 3D electromagnetic diffusion: Journal of Open Source Software, **4**, 1463, doi: 10.21105/joss.01463.

Werthmüller, D., R. Rochlitz, O. Castillo-Reyes, and L. Heagy, 2021, Towards an open-source landscape for 3-D CSEM modelling: Geophysical Journal International, **227**, 644–659, doi: 10.1093/gji/ggab238.

Willems, C. J., A. Vondrak, H. F. Mijnlieff, M. E. Donselaar, and B. M. van Kempen, 2020, Geology of the Upper Jurassic to Lower Cretaceous

geothermal aquifers in the west Netherlands basin — An overview: Netherlands Journal of Geosciences, **99**, e1, doi: 10.1017/njg.2020.1.
Wu, H., P. Fu, A. J. Hawkins, H. Tang, and J. P. Morris, 2021, Predicting thermal performance of an enhanced geothermal system from tracer tests in a data assimilation framework: Water Resources Research, **57**, e2021WR030987, doi: 10.1029/2021WR030987.
Zhang, Y., F. C. Vossepoel, and I. Hoteit, 2020, Efficient assimilation of crosswell electromagnetic data using an ensemble-based history-matching framework: SPE Journal, **25**, 119–138, doi: 10.2118/193808-PA.

Biographies and photographs of authors are not available.